Photoionization of doubly-charged scandium ions

A. M. Sossah, H.-L. Zhou, and S. T. Manson*
Department of Physics and Astronomy, Georgia State University, Atlanta, Georgia 30303, USA
(Received 23 September 2008; published 11 November 2008)

Photoionization cross-section calculations are performed for the ground ($[Ne]3s^23p^63d\ ^2D^e_{3/2}$) and the first two excited states ($[Ne]3s^23p^63d\ ^2D^e_{5/2}$), ($[Ne]3s^23p^64s\ ^2S^e_{1/2}$) of doubly-charged scandium (Sc^{2+}) for photon energies from threshold to 68.0 eV. The discrete Sc^{3+} orbitals are generated using the computer program AUTOSTRUCTURE; 24 configurations are included in the configuration-interaction calculation for Sc^{3+}. In addition to the nonrelativistic (LS-coupling) *R*-matrix, we have used the relativistic (Breit-Pauli) *R*-matrix method to carry out the calculations to focus on relativistic effects. Relativistic and nonrelativistic results are compared to demonstrate the influence of relativistic effects. The prominent $3p \rightarrow 3d$ giant resonances are analyzed and identified, and our calculated positions and widths are compared with experimental results. Total oscillator strength calculations suggest that the experimental cross section is too small and should be multiplied by a factor of 1.63; with this factor, rather good agreement between theoretical and experimental cross section is found.

DOI: 10.1103/PhysRevA.78.053405 PACS number(s): 32.80.Fb, 32.80.Zb

I. INTRODUCTION

Open-shell atoms represent more than 70% of the total number of elements in the atomic periodic table, but atomic data involving the dynamics of open-shell atoms and their ions are far fewer than their proportion in the periodic table. This lack of data is mainly due to the serious challenge that both theorists and experimentalist have faced while working on open-shell atoms. Considering the whole group of open-shells atoms, open *d*- and *f*-subshell atoms and ions have drawn much less attention so far compared to open *s*- and *p*-subshell atoms. However, during the last few decades, the advent of third generation synchrotron radiation sources [1] and the extremely rapid development of computational power have produced significant advances in the investigation of dynamical atomic processes, and open *d*- and *f*-subshell atoms and ions have been subject to increasing interest both theoretically and experimentally. Among the dynamical process of interest is the response of these atoms and ions to ionizing radiation, the photoionization process, which is of interest as a fundamental process of nature, along with applications to a number of areas of science and technology, most notably the modeling of plasmas, astrophysical and otherwise.

In this work we report on the first stage of a study of the photoionization of the $3d$ transition metal atoms and ions. These atoms and ions hold particular interest owing to the open $3d$ subshell which allows the possibility of giant dipole resonances [2] resulting from $3p \rightarrow 3d\ \Delta n=0$ transitions. Our study begins with scandium, motivated by its position in the group of open $3d$-subshell elements in the periodic table. The ground state of scandium, in fact, has a single electron in the $3d$ subshell outside closed shells, $[Ar]3d4s^2$, and is the first and simplest transition metal atom. Thus an understanding of the photoionization of scandium, with a single electron in the open $3d$ subshell, can serve as a springboard to the understanding of the photoionization of all of the $3d$ transition metal atoms and ions generally.

However, the photoionization is quite complicated, owing to the proximity of the $3d$ and $4s$ levels, so that there is significant mixing in the initial state among $3d4s^2$, $3d^24s$, and $3d^3$ configurations which, in turn, leads to a plethora of final state configurations, thereby complicating the giant dipole resonances. Calculations in this energy region have been performed using various theoretical methodologies [3–5], none of which give satisfactory agreement with experiment [2,6–8]. Thus we turn to an even simpler system, the Sc^{2+} ion for the initial investigation. The Sc^{2+} system, the simplest atomic system with an open *d* shell, has a ground state structure given by $[Ar]3d$, isoelectronic to potassium, but with a valence $3d$ electron rather than a $4s$. Another reason for the choice of doubly-ionized scandium is the existence of experimental work [9,10] to benchmark the theoretical results. Note that theoretical work using both nonrelativistic and relativistic *R*-matrix methods to study Sc^{2+} has been reported [11,12], but poor agreement with experiment was found. Clearly, further theoretical study is required to bring the calculated and measured cross sections into agreement. This work is to be considered as part of a broader effort to produce accurate data in order to understand atomic processes involving open *d*-subshell atoms.

The photoionization of doubly-charged scandium, Sc^{2+} (also designated Sc III in spectroscopic notation) is given schematically as

$$Sc^{2+} + h\nu \rightarrow Sc^{3+} + e, \tag{1}$$

which is the direct photoionization pathway. In addition, however, the photoionization can proceed through an intermediate resonance; this pathway is represented as

$$Sc^{2+} + h\nu \rightarrow (Sc^{2+})^* \rightarrow Sc^{3+} + e. \tag{2}$$

While we are primarily interested in photoionization of the ground state, in this work, the initial states of Sc III considered in the nonrelativistic calculations are both the ground

*smanson@gsu.edu

 ©2008 The American Physical Society

$[Ne]3s^23p^63d\,^2D^e$ state and the excited $[Ne]3s^23p^64s\,^2S^e$ metastable state. This is because the measurements were performed upon a mixture of ground and metastable Sc^{2+} ions so both cross sections are required in order to make a meaningful comparison with experiment. In the relativistic case the initial states are the ground $[Ne]3s^23p^63d\,^2D^e_{3/2}$ plus the first two excited states $[Ne]3s^23p^63d\,^2D^e_{5/2}$ and $[Ne]3s^23p^64s\,^2S^e_{1/2}$. The states of the final state ion, Sc^{3+} or Sc IV, are known in *R*-matrix language as the target states, with $N=18$ electrons in this case; these are combined with the free electron to form the total final state, an $N+1=19$ electron system. By dipole selection rules, the total final state (target state+unbound electron) can have (nonrelativistic symmetries) $^2P^o$, $^2D^o$, and $^2F^o$, i.e., the nonrelativistic allowed transitions are given by

$$^2D^e \rightarrow {}^2P^o, {}^2D^o, {}^2F^o,$$

$$^2S^e \rightarrow {}^2P^o. \tag{3}$$

In the relativistic case, transitions (3) become

$$^2D^e_{3/2} \rightarrow {}^2P^o_{1/2}, {}^2P^o_{3/2}, {}^2D^o_{3/2}, {}^2D^o_{5/2}, {}^2F^o_{5/2},$$

$$^2D^e_{5/2} \rightarrow {}^2P^o_{3/2}, {}^2D^o_{3/2}, {}^2D^o_{5/2}, {}^2F^o_{5/2}, {}^2F^o_{7/2},$$

$$^2S^e_{1/2} \rightarrow {}^2P^o_{1/2}, {}^2P^o_{3/2}. \tag{4}$$

The target state (Sc^{3+}) orbitals, in the present work, are obtained by using the program AUTOSTRUCTURE [13,14]. The target state wave functions and their energy levels are determined from configuration-interaction (CI) calculations that involved 24 configurations consisting of a combination of 13 orbitals among which eight are spectroscopic orbitals. The nonrelativistic (LS-coupling scheme) and the relativistic (Breit-Pauli) *R*-matrix methods [14,15] are employed to carry out the photoionization cross-section calculations. In addition to the calculations, the resonances in the region of the giant $3p \rightarrow 3d$ excitations are analyzed (position, width, and identification) using the Quigley-Berrington (QB) code [16–18]. Theoretical photoionization cross section and resonance analysis results are compared with available experimental data [9,10].

II. THEORY AND METHOD OF CALCULATION

To consider the photoionization of an $N+1$ electron system, we start with the wave functions of the states of the *N*-electron final state system (known as target states for historical reasons) [15], constructed by introducing a set of (target) states, and possibly pseudostates, Φ_i, that are usually written as a configuration-interaction (CI) expansion in terms of some basis configuration functions φ_i,

$$\Phi_i(x_1,x_2,\ldots,x_N) = \sum_k b_{ik}\phi_k(x_1,x_2,\ldots,x_N), \tag{5}$$

where $x_j=r_j\sigma_j$ stands for the spatial position and spin of the *j*th electron, and b_{ik} are the φ_i configuration mixing coefficients. The configuration functions φ_i are constructed from a bound orbital basis set consisting of self-consistent field (SCF) orbitals plus some additional pseudo-orbitals included to model electron correlation effects. For a given φ_i configuration function, each one-electron orbital is a product of a radial function, a spherical harmonic, and a spin function. The target states of Sc IV (Sc^{3+}) orbitals were generated using the code AUTOSTRUCTURE [13,14]. Each of the single-particle spectroscopic orbitals $(1s,2s,2p,3s,3p,3d,4s,4p)$ and the pseudo-orbitals $(4\bar{d},4\bar{f},5\bar{s},5\bar{p},5\bar{d})$ radial wave functions was determined using the Thomas-Fermi statistical model radial functions calculated within the program. Using these orbitals, a configuration-interaction (CI) expansion of the Sc IV configuration functions to obtain the *N*-electron target states was performed. The set of configuration functions included five spectroscopic configurations, $3s^23p^6$, $3s^23p^53d$, $3s^23p^54s$, $3s^23p^54p$, and $3s3p^63d$, and correlation configurations that, to begin with, included all one- and two-electron replacements of the $n=3$ orbitals of the ground state of Sc^{3+}. To make the subsequent photoionization calculation more tractable, correlation configurations with very small coefficients in the CI expansions were removed, leaving us with 19 correlation configurations. Specifically, the correlation configurations included are $3s^23p^54d$, $3s^23p^54f$, $3s^23p^55s$, $3s^23p^55p$, $3s^23p^55d$, $3s^23p^43d^2$, $3s^23p^43d4p$, $3s^23p^44s4p$, $3s^23p^43d5p$, $3s^23p^44s5p$, $3s^23p^44p4d$, $3s^23p^43d4f$, $3s^23p^44s4f$, $3s^23p^44p4f$, $3s^23p^33d^3$, $3s3p^53d^2$, $3s3p^53d4s$, $3s3p^53d4p$, and $3s3p^43d^3$. Thus, a total of 24 configurations corresponding to 558 LS terms were included in the nonrelativistic calculation; for the relativistic (BP) calculation, the relativistic spin-orbit, Darwin and mass correction terms were added to the Hamiltonian and the resulting CI yielded LSJ terms constructed from the LS terms.

To get some idea of the accuracy of the *N*-electron target state energies, the calculated and (*J*-averaged) experimental (NIST) [19] energy levels relative to the ground state of Sc^{3+} states are shown in Table I, and reasonable agreement with experiment is seen.

Two separate photoionization cross-section calculations were performed. In the first, relativistic effects were neglected, and the calculation was carried out with the LS-coupling nonrelativistic *R*-matrix codes [14,15]. In our *R*-matrix calculations, the final $(N+1)$ electron system continuum wave function is expressed in the form

$$\psi_k(x_1,x_2,\ldots,x_{N+1}) = A\sum_{ij} c_{ijk}\Phi_i(x_1,\ldots,x_N;\hat{r}_{N+1}\sigma_{N+1})\frac{1}{r_{N+1}}u_{ij}(r_{N+1}) + \sum_j d_{jk}\chi_j(x_1,\ldots,x_{N+1}), \tag{6}$$

where the x_i denote the spatial $\hat{r}_i$ and the spin σ_i coordinates of the *i*th electron, the Φ_i are the channel functions obtained by coupling the target state and the angular and spin functions of the continuum electron to form states of the same total angular momentum and parity (and total angular momentum, *J*, in the Breit-Pauli calculation), and *A* is the antisymmetrization operator, which takes account of the exchange effects between the target electrons and the free electron. The functions u_{ij} are the continuum wave functions

TABLE I. Calculated and experimental (NIST) [19] energy levels in rydbergs of target states of Sc IV (Sc^{3+}) relative to the ground state.

Sc IV state	Calculated energy level	Experimental energy level
$3s^23p^6\ ^1S^e$	0.00000	0.00000
$3s^23p^53d\ ^3P^o$	2.18292	2.18451
$3s^23p^53d\ ^3F^o$	2.30121	2.29462
$3s^23p^53d\ ^1D^o$	2.44422	2.43695
$3s^23p^53d\ ^3D^o$	2.45179	2.44940
$3s^23p^53d\ ^1F^o$	2.46904	2.47003
$3s^23p^54s\ ^3P^o$	3.05900	3.04732
$3s^23p^54s\ ^1P^o$	3.09385	3.07537
$3s^23p^53d\ ^1P^o$	3.18474	3.14392
$3s^23p^54p\ ^3S^e$	3.35462	3.38750
$3s^23p^54p\ ^3D^e$	3.42229	3.45029
$3s^23p^54p\ ^3P^e$	3.46903	3.49331
$3s^23p^54p\ ^1P^e$	3.46290	3.49495
$3s^23p^54p\ ^1D^e$	3.45571	3.50529
$3s^23p^54p\ ^1S^e$	3.69386	3.62238
$3s3p^63d\ ^3D^e$	3.95760	3.91567
$3s3p^63d\ ^1D^e$	4.08921	4.02822

of the unbound electron, and the χ_i represent the quadratically integrable (L^2) functions, formed from the bound orbitals and included to ensure completeness of the total wave function. In the first sum in Eq. (6), only the terms arising from the spectroscopic configurations are included which abnegates the possibility of pseudoresonances. In the (purely discrete) second sum, however, all of the terms from the 24 N-electron configurations, coupled to all of the single-particle orbitals, both spectroscopic and correlation, are included in the set of χ_i. The parameters c_{ijk} and d_{jk} are calculated by diagonalizing the $(N+1)$-electron Hamiltonian within the inner region of the R-matrix box.

The initial state wave function, in each case, was constructed from the N-electron target states to include the main configuration, $3s^23p^63d$ or $3s^23p^64s$, along with all single electron promotions out the $3s$, $3p$ and the outer shell ($3d$ or $4s$), along with all double promotions of the type $3s^23p^5nln'l'$, and the important double promotions of the $3s^23p^43d^2nl$ variety. Other possible two-electron promotions were omitted to insure that the ground state was not overcorrelated as compared to the target states, i.e., to balance the calculation. The terms arising from these states formed the basis of a large CI calculation to obtain the initial state wave function. In Table II are presented the threshold energies of the two nonrelativistic states of doubly-ionized scandium (Sc^{2+}), the $[Ne]3s^23p^63d\ ^2D^e$ state and the excited $[Ne]3s^23p^64s\ ^2S^e$ metastable state, along with the corresponding three relativistic initial states, the ground state $[Ne]3s^23p^63d\ ^2D^e_{3/2}$ plus the first two (metastable) excited states $[Ne]3s^23p^63d\ ^2D^e_{5/2}$ and $[Ne]3s^23p^64s\ ^2S^e_{1/2}$. Comparing our theoretical ionization potentials with experimental data [9,10], also shown in the table, it is evident that agreement between theory and experiment is rather good.

TABLE II. Sc III (Sc^{2+}) states threshold energy in eV compared to experiment [9,10].

State	Calculation	Experiment	Error (%)	Abundance (%)
$^2D^e$	24.71	24.74	0.12	75.3
$^2S^e$	21.86	21.59	1.23	24.7
$^2D^e_{3/2}$	24.73	24.75	0.08	20.7
$^2D^e_{5/2}$	24.70	24.73	0.12	54.6
$^2S^e_{1/2}$	21.86	21.59	1.25	24.7

In both LS and BP calculations, the R-matrix box radius was 21.81 a.u. and 34 basis orbitals were used to represent the continuum for each value of the angular momentum.

The QB method [16–18] is adopted in this work to determine the resonance energies and widths. The QB method works in the RMATRIX environment; the reactance matrix K is computed by matching the inner-region radial functions to $n \times n_0$ linear combinations of the outer-region radial functions for n_0 open channels (n is the total number of channels retained in the close-coupling expansion). Diagonalizing the K–matrix in open-channel space leads to K_{00}, with eigenvalues λ_i; the eigenphase for each channel is given by

$$\delta_i = \tan^{-1} \lambda_i, \quad i = 1, n_0 \tag{7}$$

and the sum over all channels gives the eigenphanse sum δ. The resonance position is computed as the energy of the maximum gradient $d\delta/dE = \delta'$.

To calculate the resonance width with the QB method, we consider the Breit-Wigner [20] form of the eigenphase sum

$$\delta(E) = \bar{\delta}(E) + \tan^{-1} \frac{\Gamma/2}{E_r - E}, \tag{8}$$

where E_r is the resonance energy, Γ the resonance width, and $\bar{\delta}$ is the background eigenphase. Differentiating, evaluating at $E = E_r$, and assuming the background varies slowly over the resonance profile, i.e., $\bar{\delta}' \ll \Gamma^{-1}$, we get the width as

$$\Gamma = 2/\delta'(E_r), \tag{9}$$

which means at resonance the width is related to the inverse of the eigenphase derivative.

III. RESULTS AND DISCUSSION

A. Nonrelativistic (LS coupling) calculations

The experimental Sc^{2+} sample contains 75.3% of $^2D^e$ (ground level) and 24.7% of $^2S^e$ (excited level) [9,10], and those state fractions are used in determining the total photoionization cross section of Sc^{2+} to compare with experiment. We present the total photoionization cross section of Sc^{2+} as a result of combining the photoionization cross sections of the two levels using their respective abundances in the experimental Sc^{2+} sample, however, Figs. 1(a) and 1(b), respectively, illustrate the individual photoionization cross sections from excited $^2S^e$ and ground $^2D^e$ states of Sc^{2+}; since,

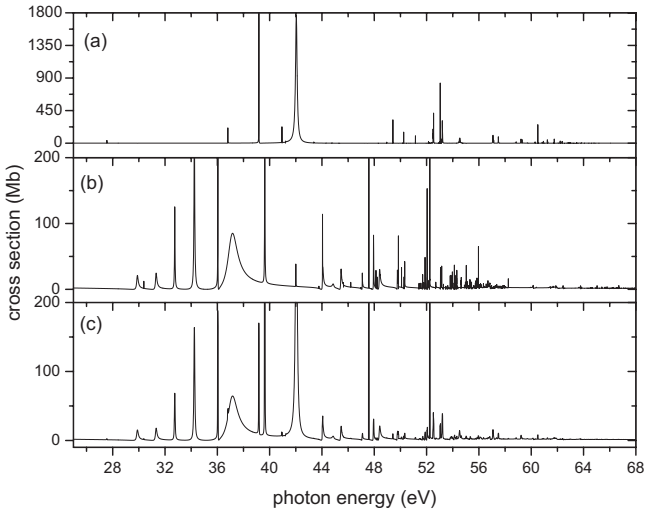

FIG. 1. Calculated photoionization cross sections of Sc^{2+}: (a) initial $^2S^e$ excited state, (b) initial $^2D^e$ ground state, and (c) total photoionization cross sections obtained from a weighted sum of (a) and (b) showing the two strongest resonances at energies 37.17 and 42.04 eV. Note the complex resonance structure at photon energies above 45 eV.

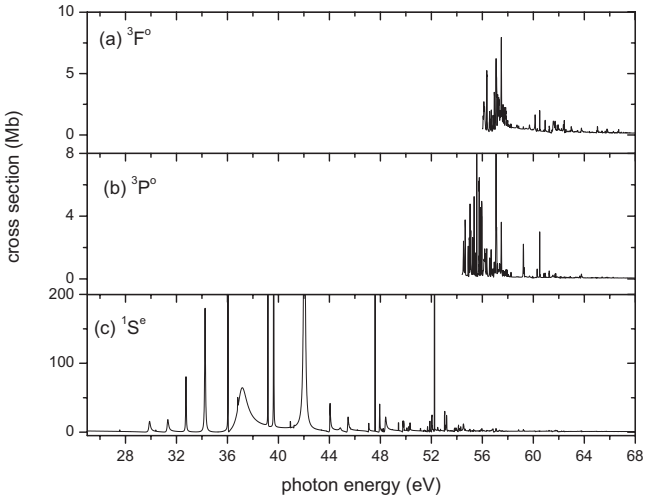

FIG. 2. Calculated photoionization cross section for the weighted sum of $^2S^e$ and $^2D^e$ initial states for the satellite transitions leaving the Sc^{3+} ion in the (a) $3s^23p^53d\ ^3F^o$ excited state and (b) $3s^23p^53d\ ^3P^o$ excited state, along with (c) the main line transition to the $3s^23p^6\ ^1S^o$ ground state of Sc^{3+}.

in both cases, the photoionization cross sections obtained using length and velocity forms agree very well, only one form (length) is displayed here and in all subsequent figures.

Figure 1(c) shows the total cross sections of the weighted mixture of ground and excited Sc^{2+} (75.3% of $^2D^e$ and 24.7% of $^2S^e$) from threshold to 68.0 eV. In the region of photon energy below 30.0 eV, there are no resonances in the total photoionization cross section; only the direct photoionization process is possible here. The threshold cross section has a value of 1.81 Mb. Between photon energy 30.0 and 50.0 eV, we have a mixture of direct nonresonant and indirect resonance processes, and it is evident that the resonance excitations are dominant in this region where the cross section can reach hundreds of Mb; this is the region of giant, $3p \rightarrow 3d$, resonances. These $3p \rightarrow 3d$ resonances are so strong because they represent $\Delta n=0$ transitions, and, since the spatial extent of a wave function is determined largely by the principal quantum number, n, the $3p$ and $3d$ wave functions occupy substantially the same region of space, resulting in significant overlap and a rather large dipole matrix element. The photoionization cross section in this region is dominated by resonances which decay *via* autoionizing processes leading to the ground $3s^23p^6\ ^1S^e$ state of Sc^{3+}. Above 50.0 eV photon energy, the photoionization cross section exhibits complex resonance structure, and this can be explained by the fact that the photon energy in this region is high enough to produce, through resonance excitation followed by autoionization, both ground and excited states of Sc^{3+} including $3s^23p^6\ ^1S^e$, $3s^23p^63d\ ^3P^o$, $3s^23p^53d\ ^3F^o$, etc., i.e., ionization plus excitation.

It is worth noting that most of the characteristics of the Sc^{2+} photoionization cross-section spectrum originate from the ejection of the $3d$ electron (or $4s$ for the excited state), leading to the ground state of the target, $3s^23p^6\ ^1S^e$. Up to a photon energy of 54.40 eV, only this channel is open; consequently other channels play minor roles in defining the photoionization cross section in the energy range considered in this work (threshold to 68.0 eV). Figure 2 is illustrative of the importance of the main line $3s^23p^6\ ^1S^e$ [Fig. 2(c)] compared to the satellite lines $3s^23p^53d\ ^3P^o$ and $3s^23p^53d\ ^3F^o$ [Figs. 2(b) and 2(a)]. Note particularly the vertical scales of Figs. 2(a) and 2(b) as compared to Fig. 2(c).

Figure 3 shows comparison between our LS results and the experimental data [9,10] for photon energies from 29 to 53.0 eV for the weighted average of $^2D^e$ and $^2S^e$ initial states. The theoretical results have been broadened by a

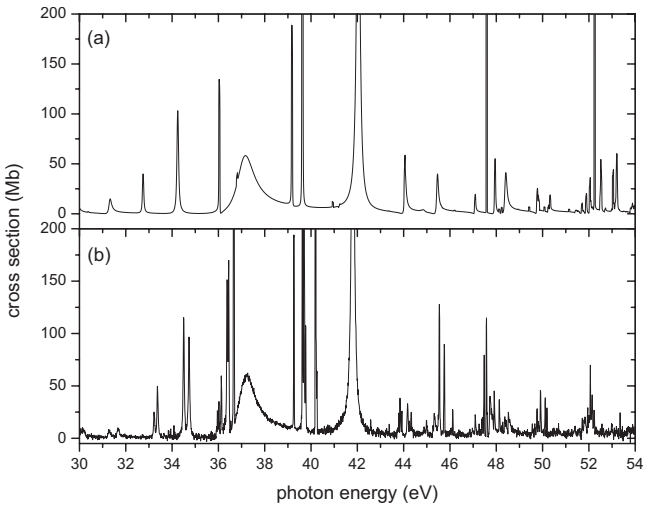

FIG. 3. Sc^{2+} photoionization cross sections from 29 to 53.0 eV for a weighted average of $^2D^e$ and $^2S^e$ initial states; (a) theory (LS-coupling) and (b) modified experiment [9,10]. Note the difference between the two spectra due to the absence of the spin-orbit interaction from the theoretical calculation. The experimental cross section has been multiplied by a factor of 1.63 for reasons discussed below.

TABLE III. Theoretical and experimental resonance energies E_{res} (eV), widths Γ (meV), and the corresponding transitions.

This calculation			Experiment	
E_{res}	Γ	Transition	E_{res}	Γ
29.89	143.5	$^2D^e \rightarrow 3p^5 3d^2(^1G)\ ^2F^o$	30.03	142
31.33	115.7	$^2D^e \rightarrow 3p^5 3d^2(^1D)\ ^2F^o$	31.66	116
34.25	64.5	$^2D^e \rightarrow 3p^5 3d(^3F)4s\ ^2F^o$	34.73	53
36.05	3.4	$^2D^e \rightarrow 3p^5 3d(^1F)4s\ ^2F^o$		
37.17	850.4	$^2D^e \rightarrow 3p^5 3d^2(^3F)\ ^2F^o$	37.13	847
44.04	8.6	$^2D^e \rightarrow 3p^5 3d(^3P)4d\ ^2P^o$		
44.07	75.5	$^2D^e \rightarrow 3p^5 3d(^3P)4d\ ^2F^o$		
32.75	46.1	$^2D^e \rightarrow 3p^5 3d(^3P)4s\ ^2P^o$	33.22	48
39.63	4.5	$^2D^e \rightarrow 3p^5 3d^2(^3P)\ ^2P^o$	39.63	4.6
42.00	6.5	$^2D^e \rightarrow 3p^5 3d^2(^1S)\ ^2P^o$		
36.81	4.5	$^2S^e \rightarrow 3p^5 3d^2(^3P)\ ^2P^o$		
39.18	6.5	$^2S^e \rightarrow 3p^5 4s^2(^1S)\ ^2P^o$	39.26	6.0
42.04	146.6	$^2S^e \rightarrow 3p^5 3d(^1P)4s\ ^2P^o$	41.80	148

40 meV width Gaussian to account for experimental resolution. The two strongest and broadest resonances of Sc^{2+} arise from $^2D^e$ and $^2S^e$ symmetries, and are located, respectively, at 37.17 and 42.04 eV, as seen in Fig. 3(a). Experimental results [9,10] showed those resonances were positioned at 37.13 and 41.80 eV [see Fig. 3(b)]. Since this calculation is a nonrelativistic operation (LS-coupling), relativistic effects, such as fine structure splitting, are not included, and the absence of the spin-orbit interaction term in the calculation can be observed in Fig. 3(a) where the theoretical photoionization cross section spectrum does not show any splitting. Above 45.0 eV both photoionization cross-section spectra 3(a) and 3(b) reveal differences even though they are less clear than in lower photon energies. Despite the use of the nonrelativistic *R*-matrix method in this first part of this work, our results reproduce experimental results better than any previous theoretical works [11,12] to the best of our knowledge; particularly if we consider the most prominent resonance positions. Deviations obtained here are smaller than those in previous theoretical calculations [11,12], relativistic or nonrelativistic. As far as absolute magnitudes are concerned, for reasons that shall be discussed below, we believe that the reported experimental cross sections are too small by a factor of 1.63. Thus the experimental cross section shown in Fig. 3 has been multiplied by that factor. With the factor, the dominant resonances in the 37 and 42 eV regions are seen to be in excellent agreement.

The QB methodology is used to analyze resonances in terms of energies, widths, and transitions. The results of our calculations are compared in Table III with the experimental data [9,10]. The resonance widths obtained in our calculation are in good agreement with experimental data, as seen in Table III. For example, the two strongest photoionization resonances have theoretical widths of 864.5 and 146.6 meV, and the corresponding experimental widths are 850 and 148 meV, respectively. In the theoretical resonance structure, we observe various widths from very narrow (3.4 meV) to very broad (850.0 meV). Since the nonrelativistic LS calculation omits fine structure splittings, our major resonance structure and identification, in the region of giant resonances, appear simpler than experimental [9,10]. For the ground state Sc^{2+} ($^2D^e$), nine resonances have been identified in the photon energies from 29 to 45 eV [Table III and Fig. 4(b)]. The spectrum of the excited state Sc^{2+} ($^2S^e$) shows less complexity than the $^2D^e$ case, and we only have three resonances between 30 and 45 eV [Table III and Fig. 4(a)].

Many resonances in the photoionization cross section exhibit an asymmetric shape, i.e., a Fano profile; this is due to the interference between the direct photoionization channels and the resonant channels. Figure 4 also shows that the two

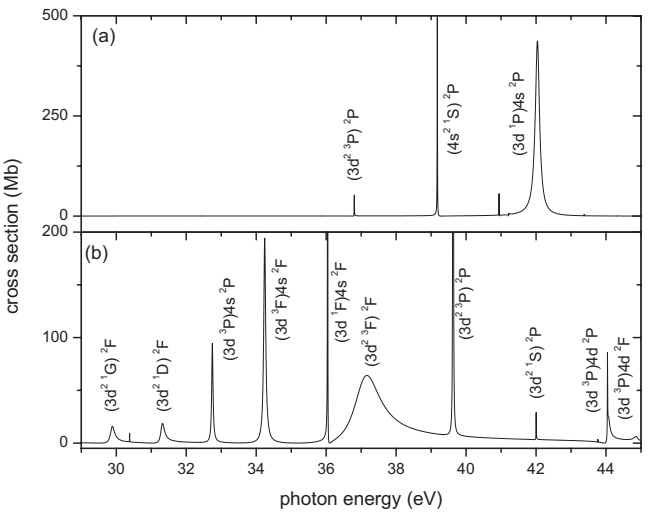

FIG. 4. Calculated (LS) Sc^{2+} photoionization cross section and resonance identifications between 29 and 45 eV for (a) initial $^2S^e$ state and (b) initial $^2D^e$ state. Both plots appear simpler than the experimental curves because of the absence of fine-structure splittings in these LS calculations. For simplicity $3p^5$ is omitted from each of the resonance designations.

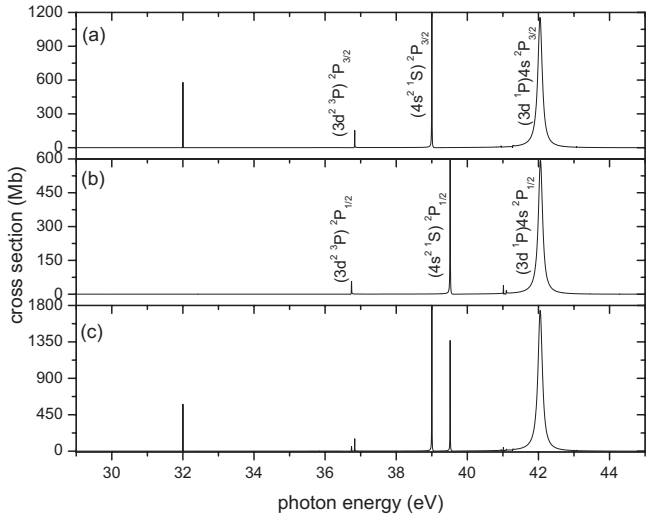

FIG. 5. Calculated Breit-Pauli photoionization cross sections of the excited $^2S^e_{1/2}$ state of Sc^{2+} showing (a) the partial cross section to the $j=3/2$ final state, (b) the partial cross section to the $j=1/2$ final state, and (c) the total $^2S^e_{1/2}$ cross section, dominated by the resonance at 42.04 eV. For simplicity $3p^5$ is omitted from each of the resonance designations.

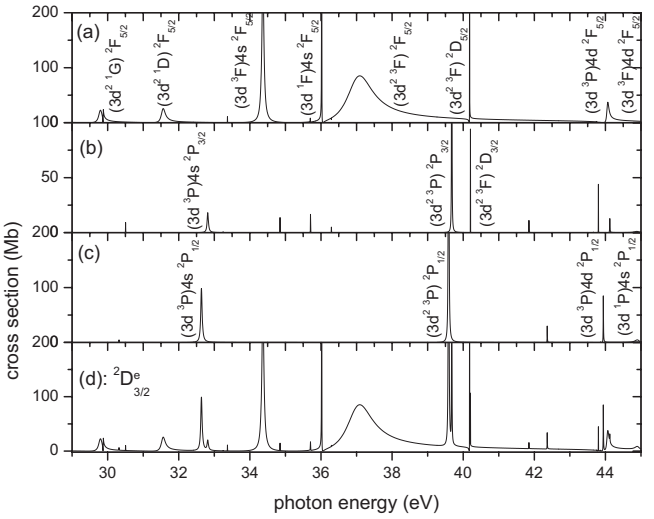

FIG. 6. Calculated Breit-Pauli photoionization cross sections of the ground $^2D^e_{3/2}$ state of Sc^{2+} showing (a) the partial cross section to the $j=5/2$ final state, (b) the partial cross section to the $j=3/2$ final state, (c) the partial cross section to the $j=1/2$ final state, and (d) the total $^2D^e_{3/2}$ cross section, dominated by the $3p^53d^2\ (^3F)\ ^2F^o_{5/2}$ resonance at 37.10 eV. For simplicity $3p^5$ is omitted from each of the resonance designations.

strongest resonances have great differences in their shapes. The $^2D^e \rightarrow 3p^53d(^3F)4s\ ^2F^o$ resonance in Fig. 4(b) is highly asymmetric while the transition $^2S^e \rightarrow 3p^53d(^1P)4s\ ^2P^o$ in Fig. 4(a) has a nearly symmetric line shape; this occurs because the underlying continuum is so small for the $^2S^e$ initial state, a $4s \rightarrow \varepsilon p$ transition, as opposed to the much larger $3d \rightarrow \varepsilon f$, εp continuum cross section for the $^2D^e$ initial state.

B. Relativistic (Breit-Pauli) calculations

When the spin-orbit interaction is considered, the experimental Sc^{2+} ion beam [9,10] consists of three components, presented in Table II; 24.7% $^2S^e_{1/2}$, 20.7% $^2D^e_{3/2}$, and 54.6% $^2D^e_{5/2}$. In the nonrelativistic case, discussed above, the ^2D fractions were simply combined. These fractions are used to obtain the theoretical total photoionization cross section for Sc^{2+} for a meaningful comparison with experiment. The calculated relativistic (Breit-Pauli) cross sections for the photoionization of the Sc^{2+} $^2S^e_{1/2}$ initial state is shown in Fig. 5. The individual $^2S^e_{1/2} \rightarrow {}^2P^o_{3/2}$ and $^2S^e_{1/2} \rightarrow {}^2P^o_{1/2}$ cross sections are presented in Figs. 5(a) and 5(b), respectively, while the total is given in Fig. 5(c). As in the nonrelativistic case, the photoionization spectrum is dominated by autoionizing resonances. Among the more important resonances are $^2S^e_{1/2} \rightarrow 3p^54s^2(^1S)^2P^o_{3/2}$ [Fig. 5(a)] and $^2S^e_{1/2} \rightarrow 3p^54s^2(^1S)^2P^o_{1/2}$ [Fig. 5(b)] located at 39.01 and 39.52 eV, respectively; experimentally [9,10], their positions are 39.26 and 39.77 eV, which means both resonances are shifted to lower energy by about 0.25 eV. These are among the largest deviations between theory and experiment found, in terms of resonance energies. However, the calculated relativistic energy splitting between these two resonances of 0.51 eV agrees exactly with experiment. Both resonances arise from the splitting of the LS resonance shown in Fig. 4(a) at 39.18 eV, identified in LS-coupling as $^2S^e \rightarrow 3p^54s^2(^1S)^2P^o$. Dominating the $^2S^e_{1/2}$ cross section, however, are clearly the giant $3p \rightarrow 3d$ resonances identified as $^2S^e_{1/2} \rightarrow 3p^53d(^1P)4s\ ^2P^o_{3/2}$ in Fig. 5(a) and $^2S^e_{1/2} \rightarrow 3p^53d(^1P)4s\ ^2P^o_{1/2}$ in Fig. 5(b); their positions and widths are 42.04 eV and 144 meV, and 42.06 eV and 138 meV, respectively. Although the relativistic interactions cause a splitting of these two resonances, the splitting is so much smaller than the widths that it is unobservable. Experimentally, the sum of these resonances is found at 41.80 eV with a width of 148 meV. Thus the theoretical resonance energy is again too high by about 0.25 eV, but the width is in excellent agreement with experiment.

The Breit-Pauli results for the photoionization of the ground $^2D^e_{3/2}$ state of Sc^{2+} are presented in Fig. 6. Note that, in the relativistic realm, L is no longer a good quantum number so that the final states of the system, the Sc^{+3} ion plus photoelectron, can be characterized only by total angular momentum, j, strictly speaking. Thus, from the $^2D^e_{3/2}$ ground state, transitions to final states with $j=5/2$, $3/2$, and $1/2$ are allowed, and these cross sections are shown in Figs. 6(a)–6(c), respectively; the total $^2D^e_{3/2}$ photoionization cross section is shown in Fig. 6(d). Resonances are seen to dominate the cross section, although the direct nonresonant photoionization channel is strong enough for interference to occur and produce the asymmetric line shapes, Fano profiles, observed in the cross sections [Figs. 6(a) and 6(d)]. The most prominent resonance is located at 37.10 eV with 837 meV width, and it is due to transition $^2D^e_{3/2} \rightarrow 3p^53d^2\ (^3F)\ ^2F^o_{5/2}$. This decays *via* a super-Coster-Kronig transition $(3p^53d^2 \rightarrow 3p^6 + e^-)$ that is also observed in the photoionization cross sections of the $[Ne]3s^23p^63d\ ^2D^e$ states of metastable Ca^+ and ground state Ti^{3+} [21]; as long as the excitation energy is above the $3d$ threshold, this channel is open and results in this broad giant resonance. When the excitation energy is below the $3d$ ionization threshold, this decay channel is

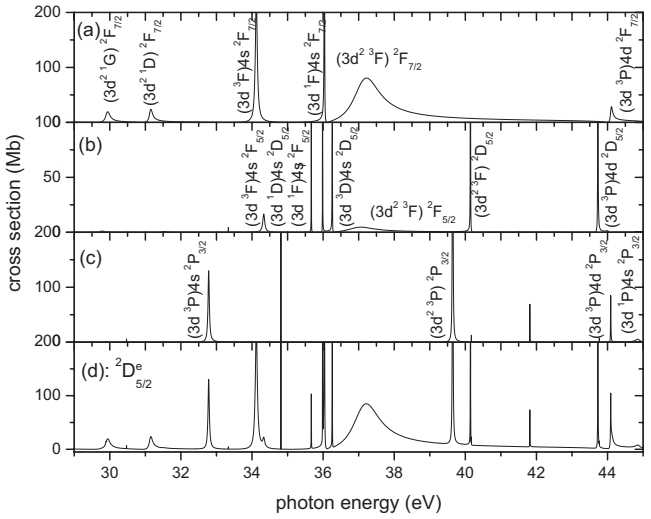

FIG. 7. Calculated Breit-Pauli photoionization cross sections of the ground $^2D^e_{3/2}$ state of Sc^{2+} showing (a) the partial cross section to the $j=7/2$ final state, (b) the partial cross section to the $j=5/2$ final state, (c) the partial cross section to the $j=3/2$ final state, and (d) the total $^2D^e_{3/2}$ cross section, dominated by the $3p^53d^2\ (^3F)\ ^2F^o_{7/2}$ resonance at 37.22 eV. For simplicity $3p^5$ is omitted from each of the resonance designations.

closed, and this is the case for *K*-like higher-*Z* ions starting with V^{4+}. Our theoretical results show good agreement with experimental data [9,10] that place this resonance at 37.14 eV with 847 meV width. An illustration of the relativistic effects in the $^2D^e_{3/2}$ cross section is the splitting leading to the transitions $^2D^e_{3/2}\rightarrow 3p^53d^2\ (^3P)\ ^2P^o_{1/2}$ and $^2P^o_{3/2}$ at 39.59 eV [Fig. 6(c)] and 39.68 eV [Fig. 6(b)], respectively; both correspond to the LS-coupling transition $^2D^e\rightarrow 3p^53d^2\ (^3P)\ ^2P^o$ at 39.63 eV seen in Fig. 4(b).

In Fig. 7, the calculated Breit-Pauli results are presented for the corresponding photoionization cross section for the excited $^2D^e_{5/2}$, where the partial cross sections for $j=7/2$, 5/2, and 3/2 final states are shown in Figs. 7(a)–7(c), respectively. The total photoionization cross section for the $^2D^e_{5/2}$ initial state is shown in Fig. 7(d). The strongest resonance, located at 37.22 eV in Fig. 7(a), and due to transition $^2D^e_{5/2}\rightarrow 3p^53d^2\ (^3F)\ ^2F^o_{7/2}$, has a width of 852.4 meV (847 meV experimentally); it is of substantially the same width as the corresponding $^2D^e_{3/2}$ resonance (837 meV). Another noteworthy feature of the $^2D^e_{5/2}$ cross section is the relativistic (spin-orbit) splitting of LS resonances. To the LS-coupling transition $^2D^e\rightarrow 3p^53d\ (^3P)4d\ ^2F^o$ correspond two relativistic transitions, $^2D^e_{5/2}\rightarrow 3p^53d\ (^3P)4d\ ^2F^o_{5/2}$, seen in Fig. 7(b) at 43.98 eV, and $^2D^e_{5/2}\rightarrow 3p^53d\ (^3P)4d\ ^2F^o_{7/2}$, seen in Fig. 7(a) at 44.11 eV. Additional fine structure splitting is illustrated in transitions $^2D^e_{5/2}\rightarrow 3p^53d^2\ (^3P)\ ^2P^o_{3/2}$ in Fig. 7(c) at 39.65 eV, and $^2D^e_{3/2}\rightarrow 3p^53d^2\ (^3P)\ ^2P^o_{3/2}$ in Fig. 6(b) at 39.68 eV; these transitions are to the same resonance from differing initial states. Thus the splitting is exactly the fine structure splitting between $^2D^e_{3/2}$ and $^2D^e_{5/2}$ which is 0.03 eV in this calculation (0.024 eV in the experiment [9,10]). A similar situation arises for the transitions to the $3p^53d\ (^3P)4s\ ^2P^o_{3/2}$ resonance from the $^2D^e_{3/2}$ and $^2D^e_{5/2}$ initial states; again these transitions are separated by 0.03 eV.

Note that, in the results for the relativistic calculations, there exist resonances identified as $^2D^e_{5/2}\rightarrow 3p^53d\ (^3D)4s\ ^2D^o_{5/2}$, seen in Fig. 7(b) at 36.26 eV, $^2D^e_{3/2}\rightarrow 3p^53d^2\ (^3F)\ ^2D^o_{5/2}$, seen in Fig. 6(a) at 40.18 eV, $^2D^e_{3/2}\rightarrow 3p^53d^2\ (^3F)\ ^2D^o_{3/2}$ seen in Fig. 6(b) at 40.20 eV, and $^2D^e_{5/2}\rightarrow 3p^53d^2\ (^3F)\ ^2D^o_{5/2}$, seen in Fig. 7(b) at 40.15 eV, their narrow widths notwithstanding; those resonances mark an important difference between relativistic and nonrelativistic calculations. Specifically, they are forbidden in the nonrelativistic LS calculation because the $^2D^e\rightarrow {}^2D^o$ channel only opens at a photon energy of 54.48 eV. Below this energy, in the 29.0–45.0 eV range, the only open channels for the photoionization of the $3p^63d\ ^2D$ initial state $3p^6\varepsilon p\ ^2P$ and $3p^6\varepsilon f\ ^2F$. As mentioned above, however, in the relativistic regime, *L* is no longer a good quantum number; only total angular momentum *j* is. Thus the (LS-forbidden) $^2D_{3/2}$ and $^2D_{5/2}$ final states of the Sc^{3+} ion-plus-photoelectron system are not pure, but are mixed with the (LS-allowed) $^2P_{3/2}$ and $^2F_{5/2}$, respectively, i.e., mixed with allowed states of the same *j*. These resonances demonstrate that relativistic interactions affect the results beyond shifts and splittings of resonances and thresholds.

A summary of positions, widths, and identifications of the major resonances obtained in the relativistic Breit-Pauli calculation is given in Table IV, along with a comparison with available experimental data [9,10]. In general the agreement is quite good, especially for the $3p^53d^2$ resonances as regards both position and width. Note that some of the resonances listed in Table IV can be reached by more than one initial state in the experimental mixture, and one, $3d^2(^3P)$, $^2P_{3/2}$, can be excited from all three initial states. They are listed more than once for purposes of comparison with the experimental results. That they are listed at a different photon arises simply because each of the three initial states has a different ionization energy so that differing photon energies are required from each of these initial states to excite a particular resonance, i.e., the difference in the resonance energies for a given resonance state in the table is just the difference in the binding energies of the initial states of the transitions.

A very useful check upon the magnitude of photoionization cross sections is the Thomas-Reiche-Kuhn sum rule [22] which states that the sum of the oscillator strengths (integral over the continuum part) to all possible final states from a given initial state of an atom or atomic ion is exactly equal to the number of electrons in the initial state. It has also been found that the sum rule is true to an excellent approximation subshell by subshell [23]. Since the photoionization cross section is simply a multiplicative constant times the (differential) oscillator strength [23], the total oscillator strength represented by the photoionization cross section can be easily calculated. In the present case, it is expected that the cross section should include almost all of the strength from the $3p^6$ subshell owing to the giant $3p\rightarrow 3d$ resonances which all occur in the continuum; for the outer shell electron, on the other hand, most of the oscillator strength will likely occur in the discrete, i.e., photoexcitation rather than photoionization. Owing to these considerations, the total oscillator strength in the photoionization cross of Sc^{2+} from threshold to 68 eV should be a bit under 6, the number of $3p$ electrons. Our

TABLE IV. Theoretical (relativistic Breit-Pauli) and experimental resonance energies E_{res} (eV), widths Γ (meV), and the corresponding transitions.

This calculation			Experiment	
E_{res}	Γ	Transitions	E_{res}	Γ
36.75	5.3	$^2S^e_{1/2} \rightarrow 3d^2(^3P)\ ^2P_{1/2}$		
36.83	4.0	$^2S^e_{1/2} \rightarrow 3d^2(^3P)\ ^2P_{3/2}$		
39.52	6.3	$^2S^e_{1/2} \rightarrow 4s^2(^1S)\ ^2P_{1/2}$	39.77	6.0
39.00	7.1	$^2S^e_{1/2} \rightarrow 4s^2(^1S)\ ^2P_{3/2}$	39.26	7.2
42.06	138.0	$^2S^e_{1/2} \rightarrow 3d(^1P)4s\ ^2P_{1/2}$		
42.04	144.0	$^2S^e_{1/2} \rightarrow 3d(^1P)4s\ ^2P_{3/2}$	41.80	148
32.64	44.9	$^2D^e_{3/2} \rightarrow 3d(^3P)4s\ ^2P_{1/2}$	33.22	45
32.79	42.5	$^2D^e_{5/2} \rightarrow 3d(^3P)4s\ ^2P_{3/2}$	33.37	48
32.82	42.3	$^2D^e_{3/2} \rightarrow 3d(^3P)4s\ ^2P_{3/2}$		
39.59	5.3	$^2D^e_{3/2} \rightarrow 3d^2(^3P)\ ^2P_{1/2}$	39.63	4.6
39.65	3.9	$^2D^e_{5/2} \rightarrow 3d^2(^3P)\ ^2P_{3/2}$	39.69	3.8
39.68	3.9	$^2D^e_{3/2} \rightarrow 3d^2(^3P)\ ^2P_{3/2}$	39.71	2.6
29.88	126.2	$^2D^e_{3/2} \rightarrow 3d^2(^1G)\ ^2F_{5/2}$	30.03	142
29.95	149.6	$^2D^e_{5/2} \rightarrow 3d^2(^1G)\ ^2F_{7/2}$	30.17	142
31.57	127.2	$^2D^e_{3/2} \rightarrow 3d^2(^1D)\ ^2F_{5/2}$	31.66	116
31.16	101.5	$^2D^e_{5/2} \rightarrow 3d^2(^1D)\ ^2F_{7/2}$	31.27	111
34.37	64.9	$^2D^e_{3/2} \rightarrow 3d(^3F)4s\ ^2F_{5/2}$	34.73	53
34.13	63.1	$^2D^e_{5/2} \rightarrow 3d(^3F)4s\ ^2F_{7/2}$	34.50	44
34.34	64.9	$^2D^e_{5/2} \rightarrow 3d(^3F)4s\ ^2F_{5/2}$		
36.02	1.1	$^2D^e_{3/2} \rightarrow 3d(^1F)4s\ ^2F_{5/2}$		
36.04	5.2	$^2D^e_{5/2} \rightarrow 3d(^1F)4s\ ^2F_{7/2}$		
35.99	1.1	$^2D^e_{5/2} \rightarrow 3d(^1F)4s\ ^2F_{5/2}$		
35.66	0.8	$^2D^e_{5/2} \rightarrow 3d(^1D)4s\ ^2D_{5/2}$		
36.26	0.7	$^2D^e_{5/2} \rightarrow 3d(^3D)4s\ ^2D_{5/2}$		
37.10	837.0	$^2D^e_{3/2} \rightarrow 3d^2(^3F)\ ^2F_{5/2}$	37.13	847
37.22	852.4	$^2D^e_{5/2} \rightarrow 3d^2(^3F)\ ^2F_{7/2}$		
37.07	837.0	$^2D^e_{5/2} \rightarrow 3d^2(^3F)\ ^2F_{5/2}$		
44.06	71.6	$^2D^e_{3/2} \rightarrow 3d(^3P)4d\ ^2F_{5/2}$		
44.11	75.5	$^2D^e_{5/2} \rightarrow 3d(^3P)4d\ ^2F_{7/2}$		
43.73	8.1	$^2D^e_{5/2} \rightarrow 3d(^3P)4d\ ^2D_{5/2}$		
44.09	8.3	$^2D^e_{5/2} \rightarrow 3d(^3P)4d\ ^2P_{3/2}$		
44.84	148	$^2D^e_{5/2} \rightarrow 3d(^1P)4s\ ^2P_{3/2}$		
43.94	2.1	$^2D^e_{3/2} \rightarrow 3d(^3P)4d\ ^2P_{1/2}$		
40.18	0.7	$^2D^e_{3/2} \rightarrow 3d^2(^3F)\ ^2D_{5/2}$	40.21	0.8
40.20	0.3	$^2D^e_{3/2} \rightarrow 3d^2(^3F)\ ^2D_{3/2}$		
40.15	0.8	$^2D^e_{5/2} \rightarrow 3d^2(^3F)\ ^2D_{5/2}$	40.19	0.9

calculated oscillator strength is 5.29, which is certainly of the correct magnitude. Performing the same calculation on the experimental results, we find a measured oscillator strength of 3.24, which is too low; we cannot account for the missing oscillator strength. Thus we believe that the overall magnitude of the measured cross section is too small and should be multiplied by a factor of 5.29/3.24=1.63 to bring the oscillator strength to a reasonable value. In our comparison with experimental cross sections, therefore, we have used this modified experimental cross section.

The comparison between the two theoretical calculations (nonrelativistic and relativistic) and the (modified) experimental data from 29 to 53 eV is shown in Fig. 8. The Breit-Pauli calculations [Fig. 8(b)] give good agreement with experimental data [9,10] [Fig. 8(c)] while the LS coupling calculations [Fig. 8(a)], in spite of the absence of fine structure splitting, give a fairly accurate idea about positions of major resonances in the cross section. The most important features of the Sc^{2+} photoionization experimental results [Fig. 8(c)] are well-reproduced by the present Breit-Pauli

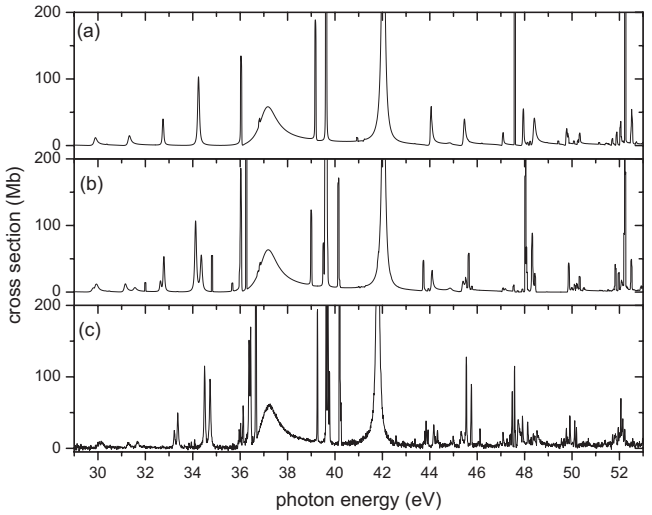

FIG. 8. Sc^{2+} photoionization cross sections from 29 to 53.0 eV for a weighted average of $^2D^e$ and $^2S^e$ initial states; (a) theory (LS-coupling), (b) theory (relativistic Breit-Pauli), and (c) modified experiment [9,10]. The experimental cross section has been multiplied by a factor of 1.63 for reason discussed in text.

calculations [Fig. 8(b)], although small deviations in some resonance positions remain.

IV. CONCLUSION

Photoionization calculations have been performed for Sc^{2+}, the simplest atomic system containing a *d*-electron in the ground state. The calculations have been performed using the nonrelativistic (LS-coupling) and the relativistic (Breit-Pauli) *R*-matrix methods. Our results showed that the cross section is dominated by $3p \rightarrow 3d$ giant resonances. Rather good agreement was found between experiment and theory for the positions and widths of the major resonances. The overall magnitudes of the experimental and theoretical cross sections differed considerably, and a sum rule analysis seemed to indicate that the experimental cross section was too small; multiplication by a factor of 1.63, indicated by the sum rule analysis, brought experiment and theory into quite good agreement.

The effects of relativistic interactions (notable the spin-orbit effect) were highlighted by comparison of the nonrelativistic and relativistic calculations. It was found that, in addition to shifts and splitting of various resonances, relativistic effects were important in that various transitions that were forbidden at the LS-coupling level of calculation became possible when relativistic interactions were introduced. Nevertheless, our results show that the nonrelativistic *R*-matrix method using LS-coupling, despite the exclusion of relativistic effects, is still reasonably good for investigating atomic processes such as photoionization at intermediate *Z*. However, relativistic (Breit-Pauli or Dirac) *R*-matrix is required for good quantitative agreement with experimental data.

Finally, we reiterate that this study is an initial effort in our program to investigate the photoionization of transition metal atoms and ions. Calculations are in progress to continue along the isoelectronic sequence up to $Z=30$, and to use what we have learned in the present work to understand the photoionization of neutral Sc.

ACKNOWLEDGMENTS

This work was supported by USDOE and NASA. We would like to thank A. Hibbert for assistance and discussions concerning Sc^{3+} target orbitals, and we want to express our gratitude to N. Badnell for making available on his very comprehensive website all the codes on *R*-matrix used in this work. We would also like to thank A. Müller, R. Phaneuf, and S. Schippers for supplying their data in numerical form and for numerous discussions. The calculations were performed using the computational facilities at the National Energy Research Scientific Computing Center (NERSC).

[1] *New Directions in Research With Third-Generation Soft X-Ray Synchrotron Radiation Sources*, Vol. 254, NATO Advanced Study Institute Series E: Applied Sciences, edited by A. S. Schlachter and F. J. Wuilleumier (Kluwer, Dordrecht, 1992).
[2] B. Sonntag and P. Zimmerman, Rep. Prog. Phys. **55**, 911 (1992).
[3] Z. Altun and S. T. Manson, Europhys. Lett. **33**, 17 (1996).
[4] Z. Altun and S. T. Manson, Phys. Rev. A **59**, 3576 (1999).
[5] M. Martins, J. Phys. B **35**, L223 (2002).
[6] K. Tiedtke, Ch. Gerth, M. Martins, B. Obst, and P. Zimmermann, J. Phys. B **33**, L755 (2000).
[7] S. B. Whitfield, K. Kehoe, R. Wehlitz, M. O. Krause, and C. D. Caldwell, Phys. Rev. A **64**, 022701 (2001).
[8] S. B. Whitfield, K. Caspary, T. Myers, M. Bjelland, R. Wehlitz, J. Jiméniz-Mier, P. Olalde-Velasco, and M. O. Krause, J. Phys. B **38**, 3273 (2005).
[9] S. Schippers, A. Müller, S. Ricz, M. E. Bannister, G. H. Dunn, J. Bozek, A. S. Schlachter, G. Hinojosa, C. Cisneros, A. Aguilar, A. M. Covington, M. F. Gharaibeh, and R. A. Phaneuf, Phys. Rev. Lett. **89**, 193002 (2002).
[10] S. Schippers, A. Müller, S. Ricz, M. E. Bannister, G. H. Dunn, A. S. Schlachter, G. Hinojosa, V. Cisneros, A. Aguilar, A. M. Covington, M. F. Gharaibeh, and R. A. Phaneuf, Phys. Rev. A **67**, 032702 (2003).
[11] J. Zeng, G. Zhao, and J. Yuan, Phys. Rev. A **68**, 022714 (2003).
[12] Z. Altun and S. T. Manson, J. Phys. B **32**, L255 (1999).
[13] W. Eissner, M. Jones, and H. Nussbaumer, Comput. Phys. Commun. **8**, 270 (1974).
[14] UK APAP Codes: http://amdpp.phys.strath.ac.uk/tamoc/code.html
[15] K. A. Berrington, W. B. Eissner, and P. H. Norrington, Comput. Phys. Commun. **92**, 290 (1995).

[16] K. Berrington, L. Quigley, and J. Pelan, Comput. Phys. Commun. **114**, 225 (1998).
[17] L. Quigley and K. Berrington, J. Phys. B **29**, 4529 (1996).
[18] J. M. Ramirez and M. A. Bautista, J. Phys. B **35**, 4139 (2002).
[19] NIST: http://physics.nist.gov/PhysRefData/ASD/levels_form.html
[20] G. Breit and E. P. Wigner, Phys. Rev. **49**, 519 (1936).
[21] S. Schippers, A. Müller, R. A. Phaneuf, T. van Zoest, I. Álvarez, C. Cisneros, E. D. Emmons, M. F. Gharaibeh, G. Hinojosa, A. S. Schlachter, and S. W. J. Scully, J. Phys. B **37**, L209 (2004).
[22] H. A. Bethe and E. E. Salpeter, *Quantum Mechanics of One- and Two-Electron Atoms* (Springer-Verlag, Berlin, 1957), p. 255ff.
[23] J. Berkowitz, *Photoabsorption, Photoionization, and Photoelectron Spectroscopy* (Academic Press, New York, 1979).